Self-Poled Sausage-Like PVDF Nanowires Produced by Confined Phase Inversion as Novel Piezoelectric Nanogenerators

Hosna Soleymani, Mohammad Noormohammadi, Mohammad Almasi Kashi, Morteza Hassanpour Amiri, Jasper J. Michels,* Kamal Asadi, and Mohammad Mahdi Abolhasani*

Piezoelectric poly(vinylidene fluoride) (PVDF) nanowires are of particular interest for energy harvesting as they are ultra-sensitive to small vibrations. Here, a new, cost-effective, and scalable approach to producing PVDF nanowires with strongly enhanced power output is presented. The method combines template-wetting in cylindrical nano-confinement with anisotropic solvent-nonsolvent phase inversion to yield a fully novel nanowire morphology consisting of "sausage-like" strings of nano-domains. Dynamic numerical simulations of the phase inversion reveal the formation of these structures to be subject to a very rich and complex phenomenology. The simulated dependence of the feature size on the degree of confinement agrees with the experimentally observed trend. It is unambiguously demonstrated that the sausage-like nano-generators upsurge the power density to 280% compared to normal nanowires. Finite element modeling explains how the higher deformability of the sausage-like nanostructures gives rise to this significant enhancement in piezoelectric performance.

H. Soleymani, Dr. M. M. Abolhasani Chemical Engineering Department University of Kashan Kashan 8731753153, Iran

Dr. M. Noormohammadi, Prof. M. A. Kashi Department of Physics

University of Kashan

Kashan 87317-51167, Iran

M. H. Amiri, Dr. J. J. Michels, Prof. K. Asadi, Dr. M. M. Abolhasani

Max-Planck Institute for Polymer Research

Ackermannweg 10, 55128 Mainz, Germany

 $\hbox{E-mail: michels@mpip-mainz.mpg.de; abolhasani@mpip-mainz.mpg.de}$

Prof. K. Asadi

Department of Physics

University of Bath

Claverton Down, Bath BA2 7AY, UK

The ORCID identification number(s) for the author(s) of this article can be found under https://doi.org/10.1002/admi.202001734.

© 2021 The Authors. Advanced Materials Interfaces published by Wiley-VCH GmbH. This is an open access article under the terms of the Creative Commons Attribution License, which permits use, distribution and reproduction in any medium, provided the original work is properly cited.

The copyright line for this article was changed on 19 February 2021 after original online publication.

DOI: 10.1002/admi.202001734

1. Introduction

The Internet of Things (IoT) forms the basis for the development of smart cities with billions of sensors which monitor weather conditions, vehicular and pedestrian traffic, humans and animals' health, etc.[1] Powering billions of IoT devices with batteries is infeasible due to regular replacement/maintenance issues and batteries hardly scale with the size and weight of the sensors. Harvesting ubiquitous wasted mechanical energy from civil structures, bridges, shaking parts of motors, or even human and animal movements is a perspective for replacing batteries. Piezoelectric nanogenerators (PNGs) have the capability of converting small-scale mechanical vibrations to electricity. Besides for IoT, in particular, soft and flexible nanogenerators are of prime interest to bionic applications, such as arti-

ficial skin^[2,3] and conformable motion sensing.^[4] Nanogenerators have traditionally^[5] been demonstrated with inorganic materials, such as zinc oxide $(ZnO)^{[6,7]}$ and subsequently, gallium nitride (GaN),^[8] barium titanate $(BaTiO_3)$,^[9] and $PbZr_xTi_{1-x}O_3$ (PZT).^[10] More recently, owing to their flexibility and ease of processing, polymeric ferro/piezoelectric materials, such as nylon,^[11,12] poly(vinylidene fluoride) (PVDF),^[13,14] and poly(vinylidene fluoride-co-trifluoroethylene) (P(VDF-TrFE)),^[15–19] as well as hybrid nanocomposites^[20] have gained significant interest, not only for nanogenerators, but for printable memory devices.

PVDF is a semicrystalline, piezoelectric polymer with five different polymorphs, that is, α , β , γ , δ , and ε . $^{[21-24]}$ The desired piezoelectric β -polymorph has a large piezoelectric charge coefficient, d_{33} between -30 and -40 pV m $^{-1}$, $^{[25,26]}$ and is usually obtained by high temperature stretching (\approx 90 °C) and poling (\approx 100 MV m $^{-1}$). $^{[27]}$ In the last decade, much attention has been devoted to electrospinning and melt-spinning piezoelectric PVDF fibers. $^{[24,28-35]}$ Of these, electrospinning requires high voltages (5–50 kV) and the piezoelectric performance of the resulting nanofibers suffers from the broad distribution in fiber width. The fiber width is arguably better controlled with melt-spinning, but poling in a high electric field is necessary for an additional step. Nano-pore template-wetting is an accessible, cost-effective, and scalable alternative that directly produces



www.advmatinterfaces.de

piezoelectric nanowires with, per definition, a low width dispersity.[36] Nanowires obtained using template-wetting are highly crystalline and consequently exhibit enhanced piezoelectric properties without poling.[36-38] However, to the best of our knowledge the possibilities of the template-wetting method to reach optimal piezoelectric performance have not been exploited or even investigated. Studies concerning polymer nanowire-based nanogenerators produced via template-wetting have so far been limited to the mere demonstration of the piezoelectric properties and self-polarizability. No attempt has been dedicated to improve the performance by seeking the optimal properties from a morphological perspective.

It is well-known that the nanostructure and crystallinity of specimen of PVDF and its copolymers can be controlled by making use of the fact that the polymer is typically compatible with polar hygroscopic solvents, while at the same time exhibiting non-solvency in water. As a consequence, quenching a solutioncast PVDF film in water or a humid atmosphere leads to a phase inversion process that induces liquid-liquid and liquid-solid phase separation.^[39,40] Parameters such as humidity, quenching temperature, solvent type, and composition control the typical feature size, porosity, crystallinity, and polymorphism of the dry polymer specimen or film. Besides, phase inversion results in PVDF films with a high density of β -phase domains, although randomly oriented.^[38] In contrast, owing to its cylindrical confinement template-wetting yields highly oriented crystals.^[37,41] Hence, implementing a combination of phase-inversion and templatewetting bears the perspective for the manufacture of nanogenerators with a high density of oriented domains of the β -polymorphs, and consequently superior piezoelectric performance.

In this study, we induce phase-inversion inside the cylindrical confinement of aluminum oxide nanopores containing a solution of PVDF in dimethylformamide (DMF). Upon water ingress from the pore entrances, spatially anisotropic liquid-liquid phase separation gives rise to novel PVDF nanostructures with a "sausage-like" appearance. To unveil the phenomenology of the development of these peculiar nanostructures, we perform outof-equilibrium numerical simulations using a multi-component phase field model that takes account of the wetting preference of the pore wall by the individual blend components. The calculations reveal how the size and connectedness of the domains nontrivially depend on polymer concentration and degree of confinement. We demonstrate that the necking features in the sausagelike nanostructure enhance the power output of the nanowires by 280% compared to smooth nanowires produced in the absence of phase inversion. The considerable enhancement in performance is explained by electromechanical finite element simulations.

2. Results and Discussion

2.1. Morphology of PVDF Nanowires

We fabricate two different kinds of PVDF nanowires making use of anodic aluminum oxide (AAO) templates containing cylindrical nanopores with a defined diameter in the range 50–120 nm (see Section S1, Supporting Information). The pores are filled with a solution of the polymer in DMF and, subsequently, either immersed in water to induce phase inversion,

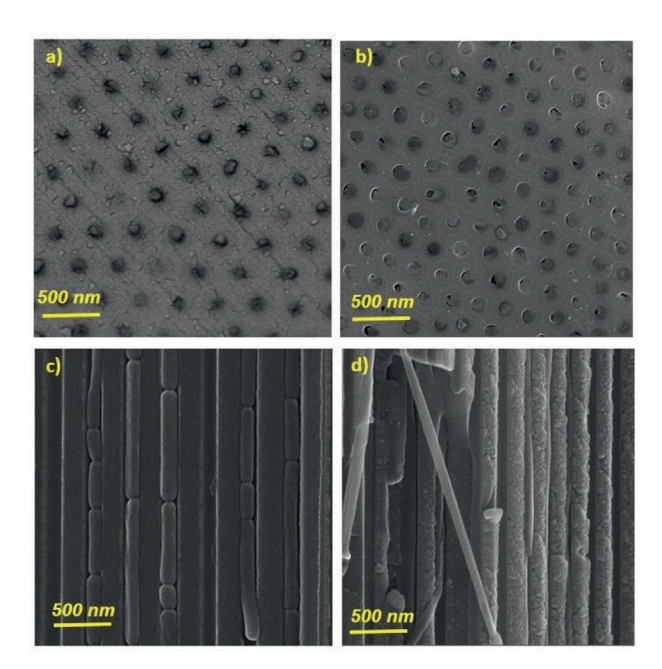


Figure 1. Top-view SEM image of the a) PVDF sausage-like nanowires (S.NWs sample), b) PVDF nanowires (NWs sample) filled AAO template. Cross-section view of c) S.NWs sample, d) NWs sample.

or immediately left to dry by letting the solvent evaporate (see Experimental Section for details). These two procedures lead to polymer nanostructures with strikingly different morphologies. Top-view SEM images of the dried PVDF-filled AAO templates (Figure 1a,b) show that, in general, in the case of the immersed templates the polymer has to some extent retracted from the pore entrance (1a), whereas for the non-immersed samples the content of the pores levels with the surface of the template.

The corresponding cross-sectional SEM images (Figure 1c.d) of broken templates clearly show a difference in the morphology of the dried nanostructures: whereas the non-immersed solution gives homogeneous nanowires upon drying, the immersed samples produce discrete domains with a "sausage-like" outward form. In most cases, these domains are mutually interconnected, but on occasions, they have either split-off from one or both of their neighbors or formed individually in the first place (see also Figure 2). As we do not have in situ information on the development of these morphologies, mechanistic aspects are hard to deduct from the SEM images alone. Below, we refer to the smooth (non-immersed) and sausage-like (immersed) samples as NW (for "nanowire") and S.NW ("S" for "sausage"), respectively.

Figure 2 shows that for the S.NW samples, the average length of the sausage-like domains increases with increasing pore diameter. We note that the size distributions have been obtained from a wide range of SEM images that are not all shown here in the main text. The SEM images in Figure 2 should hence be considered representative. We placed the full set of images in Section S2, Supporting Information. The dashed line in Figure 2a represents the best fit against an empirical linear function. The associated linear coefficient and R-square value are 5.3 and 0.9993, respectively. The shape of the S.NW samples, together with the fact that the dried domains detach from the pore-wall, suggests that during the

21967339, 2021, 5, Downloaded from https://onlinelibrary.wiely.com/doi/10.1002/admi.202001734 by Egyptian National Sti. Network (Ensinen), Wiley Online Library on [12.032023]. See the Terms and Conditions (https://onlinelibrary.wiely.com/rems-and-conditions) on Wiley Online Library for rules of use; OA articles are governed by the applicable Creative Commons Licensenses.

b) a) Experimental 800 Linear fitting

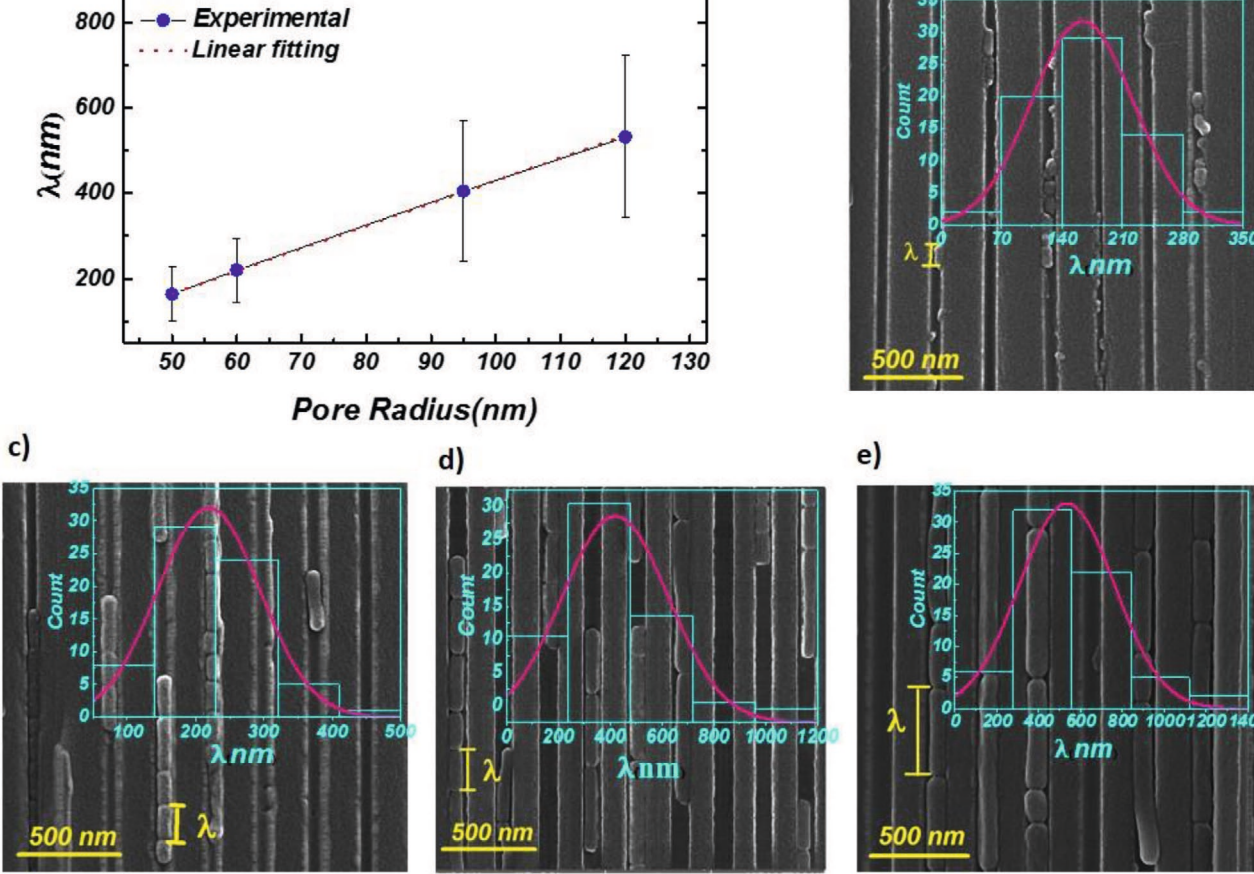


Figure 2. Domain size distribution (histograms and Gaussian fit) and mean domain size $\bar{\lambda}$ as a function of pore radius for the S.NW samples. The pores in panels b-e) are 50, 60, 95, and 120 nm, respectively. The SEM images are representative. The dashed red line in panel a) is an empirical fit against a linear function.

ingress of water, a central "plug" of a polymer-rich phase forms, surrounded by a solvent-rich phase that preferentially wets the pore wall. The necking and occasional rupture of the nanowires may be due to an instability occurring at the liquid-liquid interface running parallel to the pore wall.

As is well-known, due to the strong repulsive interaction between the polymer and water, PVDF/DMF or, equivalently, P(VDF-TrFE)/DMF, solutions undergo rapid liquid-liquid demixing upon quenching in water^[21,42,43] either by exposure to a wet atmosphere or submersion into a water bath. For this reason, this system lends itself so well for functional manufacture based on such "non-solvent-induced phase separation" (NIPS) or "phase inversion", of which microporous membranes perhaps present the best known application.^[44] In the present case, however, the pore geometry does not allow for a quick quench, as the water content in the pore only rises slowly due to the fact that ingress can only occur from the pore entrances. Establishing equilibrium between the coexisting polymer-rich and -poor phases is hence expected to (initially) occur only locally. A transient regime may arise wherein near the entrance of the pore, the mean composition resides in the miscibility gap of the phase diagram, whereas more remote from the entrance, the composition is in the single-phase region.

In order to shed light on how the tube-like confinement influences the mechanism of structure formation during lateral water ingress, we performed dynamic numerical simulations of the phase-inversion in a cross-sectional, and rotationally symmetric, cylindrical geometry. Our calculations are performed using the same multicomponent free energy-minimizing generalized diffusion approach[45-50] as we employed before for modeling the behavior of PVDF/water/ DMF ternary mixtures in thin-film and fibers.[21,42] Its description is not repeated here. The only difference is that now we solve the associated equations for the rates of change in composition in cylindrical, rather than Cartesian coordinates. For simplicity, thermal fluctuations are not taken into account. In contrast, wherein previous work the interaction of the blend components with the substrate is not considered, it proves to be essential in reproducing the shape characteristics of the structures emerging in the S.NW samples.

Since so far, a consistent formulation for the free energy contribution associated with the wall interactions in a ternary mixture is lacking in the literature, we provide some detail here. In analogy with the work by Binder et al. for a binary blend, [51,52] we assume local equilibrium at the solid surface owing to the



www.advmatinterfaces.de

fact that the relaxation due to preferential wetting is fast in comparison to the dynamics in the bulk. The equilibrium condition at the wall dictates that the surface potential arising from enrichment with one of the components is balanced by the penalties associated with local concentration gradients. However, in the case of a ternary mixture due to the incompressibility assumption, cross terms arise in the expressions for the boundary conditions at the wall. For our ternary mixture, we have: $\varphi_A + \varphi_B + \varphi_S = 1$, with subscripts A, B, and S respectively referring to polymer, water, and solvent. Treating the volume fraction of the solvent φ_S as a dependent, we obtain besides the usual no-flux constraints the following boundary conditions for the polymer and water concentration:

$$\frac{\partial \gamma}{\partial \phi_{A}^{(w)}} + b^{-3} \left(\kappa_{11} \frac{\partial \phi_{A}}{\partial r} \Big|^{(w)} + \kappa_{12} \frac{\partial \phi_{B}}{\partial r} \Big|^{(w)} \right) = 0 \tag{1}$$

$$\frac{\partial \gamma}{\partial \phi_{\rm p}^{(w)}} + b^{-3} \left(\kappa_{12} \frac{\partial \phi_{\rm A}}{\partial r} \right|^{(w)} + \kappa_{22} \frac{\partial \phi_{\rm B}}{\partial r} \right|^{(w)} = 0 \tag{2}$$

The first and second term in each of the above equations respectively represents the local exchange chemical potential due to wall-interaction and the aforementioned gradient penalty. $\phi_i^{(w)}$ is the volume fraction of the component i at the wall, γ the wall surface free energy, b a molecular length scale, r the radial coordinate, and κ_{ij} represent the gradient energy coefficients for the incompressible mixture. The latter have been evaluated in previous work. [43,50]

We assume a simple surface free energy of the form: $\gamma = k_B \, Tb^{-2} (\chi_A^{(w)} \phi_A^{(w)} + \chi_B^{(w)} \phi_B^{(w)} + \chi_S^{(w)} \phi_S^{(w)})$, with $\chi_i^{(w)}$ dimensionless (and constant) interaction parameters determining the effective interaction strength of each component with the pore wall. [50,53] In the present calculations, we assume the preference for wetting the polar aluminum oxide pore wall to be according to: water > DMF > PVDF. This is achieved by setting: $\chi_A^{(w)} = 0.025$, $\chi_B^{(w)} = -0.050$, and $\chi_S^{(w)} = -0.025$. As we will see, upon phase separation, these conditions lead to complete wetting of the pore wall by the polymer-devoid phase. Below, we will show that different conditions, that is, assuming a preference of the wall to be wetted by the polymer, indeed gives different domain shapes, which demonstrates the scope of the method and the principle possibility to steer the morphology by the wetting properties.

The wall concentrations are obtained by rewriting Equations (1) and (2) as:

$$\frac{\partial \phi_{\mathbf{A}}}{\partial r}\Big|^{(w)} = b^{3} \begin{vmatrix} \kappa_{11} & \kappa_{12} \\ \kappa_{12} & \kappa_{22} \end{vmatrix}^{-1} \left(\kappa_{12} \frac{\partial \gamma}{\partial \phi_{\mathbf{A}}^{(w)}} - \kappa_{22} \frac{\partial \gamma}{\partial \phi_{\mathbf{A}}^{(w)}} \right) \tag{3}$$

$$\frac{\partial \phi_{\rm B}}{\partial r}\Big|^{(w)} = b^3 \left| \begin{matrix} \kappa_{11} & \kappa_{12} \\ \kappa_{12} & \kappa_{22} \end{matrix} \right|^{-1} \left(\kappa_{12} \frac{\partial \gamma}{\partial \phi_{\rm A}^{(w)}} - \kappa_{11} \frac{\partial \gamma}{\partial \phi_{\rm B}^{(w)}} \right) \tag{4}$$

For completeness, but not essential to the outcome of the calculations, we implement a phenomenological long range contribution of the wall potential according to: $V_i(r) = b^{-1} \frac{\partial \gamma}{\partial \phi_R^{(w)}} \exp[a((r/R)^2 - 1)]$, with R the diameter of the pore.

The factor a determines the decay length of the potential. We use a=4, which assures the potential to decay to near zero across ≈ 10 dimensionless units of length. All distances are non-dimensionalized by normalizing over the typical interaction distance for the gradient energy, that is, the approximate size of a polymer coil. [54] Time is normalized by the typical diffusion time of a solvent molecule across the mentioned length scale. Below, non-dimensional quantities are indicated with a tilde. A somewhat different value for a does not notably affect the calculation results. Input concerning molecular size and interaction is the same as in previous work. [21,55]

We numerically simulate the phase inversion by considering a short, rotationally symmetrical, cylindrical domain (506 \times 12 and 506 × 16 grid points, respectively representing a narrow and a wide pore), containing an equilibrated solution of the polymer in the solvent. At $\tilde{t}=0$, we release a quantity of water at both sides of the domain and observe the structural changes occurring as the system relaxes towards equilibrium. Modeling the aspect ratio of the experimental pores is computationally intractable. Hence, instead of attempting to reproduce the experimental morphologies along the full extent of the pores, our calculations aim to i) provide a qualitative mechanistic explanation for how water ingress converts the homogeneous polymer solution into discrete sausage-like domains and ii) how the structuring depends on the mean polymer concentration and the pore radius, in terms of dynamics, morphology, and domain size. Although in the experiments the concentration is kept constant, we do vary it in the calculations to explore the phenomenology associated with this novel method of structuring a polymer solution beyond the experimental conditions in this work.

Figure 3, as well as Movies S1–S6, Supporting Information, gives an overview of the simulation results. The figure shows the changes in the polymer and water concentration as a function of time and position, expressing the corresponding volume fractions at the same color scale (right). Upon water ingress, the solution demixes into a polymerrich phase (yellow) surrounded by a polymer-devoid phase (dark red). The latter wets the pore wall completely. The fact that the calculations reproduce the experimentally observed sausage-like shapes supports the validity of our choice of $\chi_i^{(w)}$. The time ranges associated with the various panels in Figure 3 are comparable but not equal: typically, structure development is faster for a low concentration and/or a narrow pore.

Although the phenomenology of the process is very rich, in this more explorative work, we refrain from extensive analysis and discussion, and instead focus on a qualitative comparison with the experimental observations. Nevertheless, to demonstrate that a different choice for the wetting preference leads to different morphologies, we have taken the final snapshot of Figure 3c as a starting point for a calculation in which we assume: $\chi_{\rm A}^{(w)} = -0.05$, $\chi_{\rm B}^{(w)} = -0.025$, and $\chi_{\rm S}^{(w)} = 0.025$, that is, preferential pore wetting by the polymer (see Section S3, Figure S3, Supporting Information). As can be seen in Figure S3, Supporting Information, this leads to a loss of the sausage-like shapes, which transform into "hourglass-like" (in cross-section)

ADVANCED MATERIALS INTERFACES

www.advmatinterfaces.de

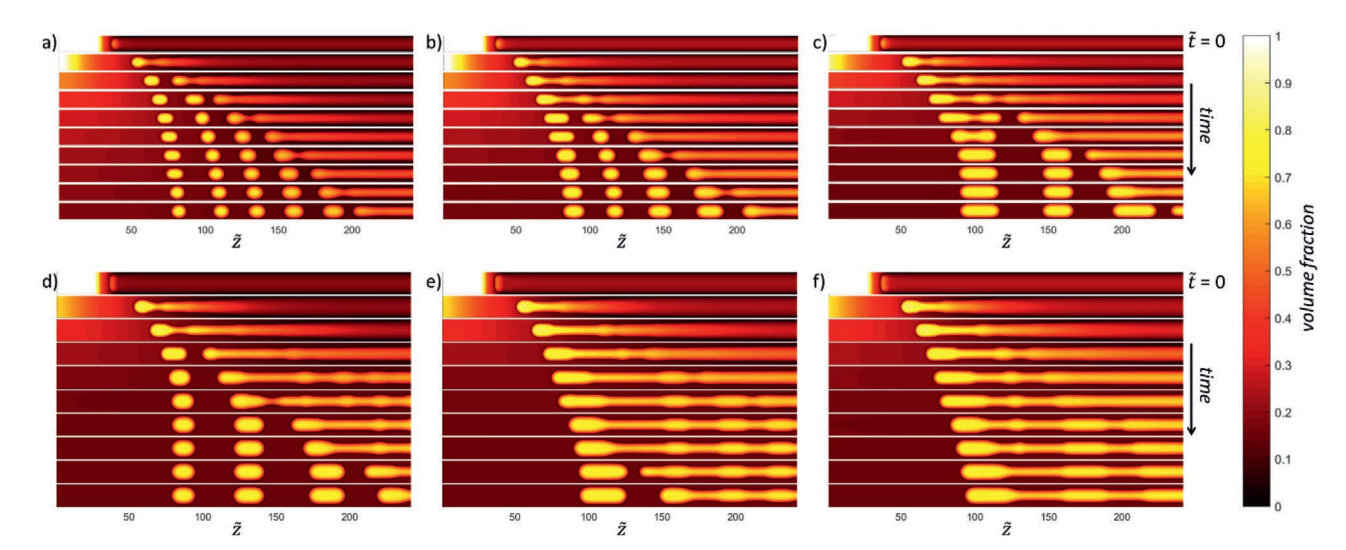


Figure 3. Numerically simulated spatial concentration fields (polymer and water) as a function of time (top to bottom in each panel (a–f)) upon ingress of water into nano-pores containing the polymer solution. Only the left part of the pores is shown. At $\tilde{t}=0$, the water is collected at the pore entrances (here), as expressed by the local color scale being white. The mean polymer concentration is from left to right: $\overline{\phi}_A=0.087$ (a,d), $\overline{\phi}_A=0.109$ (b,e), and $\overline{\phi}_A=0.120$ (c,f). Panels a–c) represent a dimensionless pore radius of: $\tilde{R}=15$, whereas panels d–f) represent $\tilde{R}=20$.

domains that partially wet the pore wall with a contact angle around 45° .

Depending on the polymer concentration and the pore radius, phase inversion is either prone to result in separate polymer-rich droplets (as in Figure 3a) or domains that remain mostly interconnected by thinner fluid "filaments" that contract over time (as in Figure 3f). We note that the evaporation/solidification stage is not considered in the numerical simulations, whereas in the experiments, during solvent evaporation, the process likely becomes frustrated while approaching global thermodynamic equilibrium by gelation or crystallization, so that the final morphology represents a "frozen" transient state. The lateral contraction of the polymer-rich phase is primarily driven by the repulsion between polymer and water. To reduce the free energy, the polymerrich phase will try to "escape" from the region where the mean water concentration is highest, that is, towards the entrance of the pore. Contributing to the contraction is the extended nature of the polymer-rich phase, which is unfavorable in terms of interfacial free energy: a droplet of a liquid phase dispersed in another liquid phase, when not spatially confined or subject to an external field, tends to become spherical rather than remain extended.

The sloping gradient in polymer concentration towards the center of the pore is a consequence of the transient nature of the process: the increase in polymer concentration due to phase inversion starts remote from the inner region of the tube, simply because the water ingresses via the pore entrances. As a result, the polymer concentration initially exhibits a broad lateral gradient, sloping off towards the central region. In due time, this situation gives way to a stage wherein the tube contains the sausage-like polymer-rich domains, dispersed in a polymer-poor phase wherein the spatial distribution of water and solvent has homogenized. The contraction of the polymer-rich phase explains the above mentioned "emptying" of the top of the pores of the S.NW samples (Figure 1a) and eventually

reduces the "filaments" to the pinches or necks observed in the stringed aggregates observed in the SEM images. The dependence of the typical domain or droplet size on the pore radius is in qualitative agreement with the experimental observations: wider pores produce a larger structure size, in principle in agreement with Rayleigh instability theory. [43] Interestingly, the same trend in the droplet size is observed when increasing the mean polymer concentration, while keeping the pore radius constant.

Close inspection of the simulation results reveals two dynamic regimes, ligated by a gradual transition. In the case of a dilute solution in strong confinement (Figure 3a), polymerrich droplets consecutively "break away" from the solution, with the point of bifurcation of the coexisting liquid phases progressing inward and remaining relatively well-defined throughout the process. As a result, the (outer) section of the pore where liquid-liquid interfaces are well-developed is at any time fairly well separated from the (inner) part containing a single (stable) phase. This regime would give rise to a morphology comprising separated domains, which would of course not be ideal for piezoelectric performance. In contrast, in the case of a concentrated solution in a wide pore (Figure 3f), demixing initially progresses quickly along a substantial section of the tube before break-up occurs. An extended liquid-liquid interface develops, along which the binodal compositions are a function of coordinate. As a consequence, gradients in Laplace pressure, as well as the contraction of the polymer-rich phase, give rise to a superposition of instabilities along the liquidliquid interface. Sequences of bulges form with a highly nontrivial transient behavior. These bulges may to some extent collapse but eventually develop into strings of interconnected domains, which may break up in a later stage, depending on the local direction of mass transport.

The fact that the SEM images of the S.NW samples reveal strings of interconnected polymer domains as well as some (partly) unconnected "sausages" (see for instance Figure 2d),



www.advmatinterfaces.de

suggests that the experimental conditions for concentration and pore radius give morphologies that are consistent with the second regime or a transitional scenario (compare with, e.g., Figure 3e). The presence of (mostly) intact structures in the S.NW specimen is, perhaps trivially, supported by the fact that we indeed measure a decent piezoelectric performance (see below). In the case where the connectivity between the domains would have been (mostly) interrupted, we would not have measured a response at all. Again, although the numerical simulations compare favorably with the experiments on multiple counts, some caution needs to be taken since the physical displacement of solid material during the evaporation stage cannot be fully excluded. Hence, from the SEM images, it is not possible to say with certainty whether two adjacent sausage-like domains have never been fully separated, or that they were fully pinched off from each other but later moved together during the drying process. Additionally, the sample preparation for SEM analysis (see Supporting Information) is not expected to leave the structures completely intact.

Using differential scanning calorimetry (DSC) analysis (see Section 4, Figure S4, Supporting Information) we determined the crystallinity of the S.NW and NW samples to be 53 and 48%, respectively. Based on these numbers, we conclude that the crystallinity of both types of wires is similar and approximately 50%. We speculate that the reason for the fact that the crystallinity of the S.NW wires is not significantly lower than for the NW specimen, might be that phase inversion in nanopores is retarded in comparison to, for instance, sudden submersion or exposure in/to water or vapor-saturated atmosphere. Hence, in this particular fabrication process, the time allowed for crystallization might be relatively uncompromised. More details on crystallinity and polymorphism are discussed in Section S4, Supporting Information, where we also have placed XRD spectra (Figure S5, Supporting Information). Despite the fact that these spectra are rather noisy due to the presence of the aluminum oxide template, the peak associated

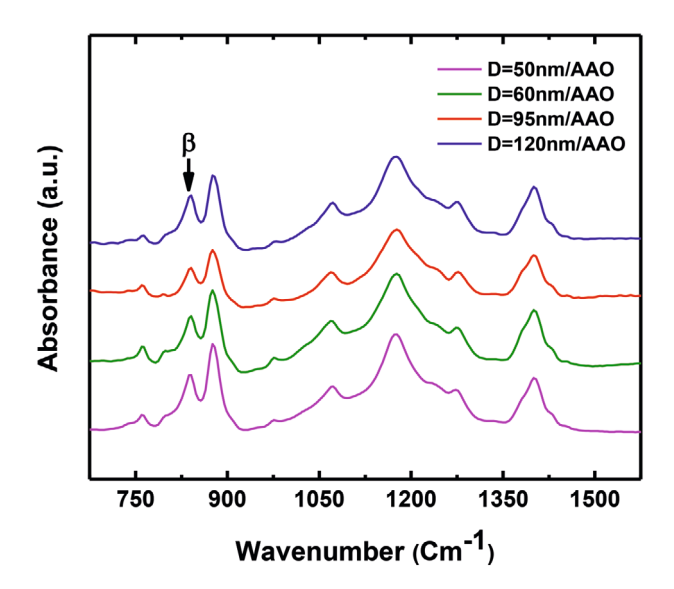


Figure 4. FTIR spectra of S.NWs Nanogenerators with different pore diameter.

with β -phase PVDF can be clearly discerned. FTIR analysis has been performed to quantify the effect of the phase inversion on β -phase formation (see **Figure 4**). Non-polar α -phase characteristics peaks at 763, 795, and 974 cm⁻¹ and polar β -phase characteristics bonds at 840 and 1277 cm⁻¹ are identified in both samples. [6] The amount of β -polymorph is calculated employing Equation (5):

$$F(\beta) = \frac{A_{\beta}}{1.26A_{\alpha} + A_{\beta}} \tag{5}$$

where $F(\beta)$ is the fraction of β phase; A_{β} and A_{α} are the absorption of peaks at 840 and 763 cm⁻¹, related to the β and α polymorphs, respectively. Interestingly, the phase inversion has increased the β -phase content from 55 to 76%. It has been reported that quenching the PVDF solution in water creates the β nuclei and consequently increases the amount of β phase. [39,56]

2.2. Energy Harvesting

Two nanogenerators have been fabricated using S.NWs and NWs samples (diameter 120 nm) and mechanically impacted (20 N) under the frequency of 5 Hz. As a promising outcome, the S.NWs nanogenerator demonstrates open circuit voltage ($V_{\rm oc}$) and short circuit currents ($I_{\rm sc}$) values of 3.12 \pm 0.07 V and 1.36 \pm 0.05 μA , higher than 1.97 \pm 0.09 V, 0.95 \pm 0.05 μA observed for NWs sample (**Figure 5**a,b). A switching-polarity test has been performed to confirm that the generated output signals arose from the piezoelectric phenomenon. Under forward connection, the nanogenerator shows a positive output signal, while if it connects to a reverse connection, an opposite output signal is observable as shown in Figure S4, Supporting Information.

To obtain the maximum output power of the nanogenerators, piezoelectric voltage across a series of resistive loads is measured. The output power is calculated using Equation (6). [57,58]

$$P = \frac{1}{t} \int_{t_1}^{t_2} \frac{V(t)^2}{R} dt \tag{6}$$

Where t_1 , t_2 , and t are the start, end and whole time of a cycle of mechanical impact. R is the resistive load which varies from 100 K Ω to10 M Ω , and V(t) is piezoelectric voltage over the impact time. Figure 4c shows the variation of power density versus load resistance. The optimum power densities of 5.55 \pm 0.08 and 1.94 \pm 0.08 μ W cm⁻² are measured for S.NWs and NWs samples, at load resistance of 1.5 M Ω , respectively.

The piezoelectric coefficient d_{33} is a measure of the ability of the PNG to convert mechanical energy into piezoelectric voltage. [56] Unfortunately, due to the fragile nature of the isolated PVDF nanowires, it proved impossible to determine an accurate value for d_{33} using conventional techniques, such as Berlincourt or laser interferometry. To still obtain a reasonable estimate, we attempted to calculate d_{33} as an intrinsic constant of the PNG following the procedure outlined in Section S6, Supporting Information. Our estimates for d_{33} are \approx 7 and \approx 18 pC N⁻¹ for NWs and S.NWs, respectively. To explore the origin of the higher d_{33} values and consequently higher power output of the sausage-like structures, finite element

21967339, 2021, 5, Downloaded from https://onlinelibrary.wiely.com/doi/10.1002/admi.202001734 by Egyptian National Sti. Network (Ensinen), Wiley Online Library on [12.032023]. See the Terms and Conditions (https://onlinelibrary.wiely.com/rems-and-conditions) on Wiley Online Library for rules of use; OA articles are governed by the applicable Creative Commons Licensenses.

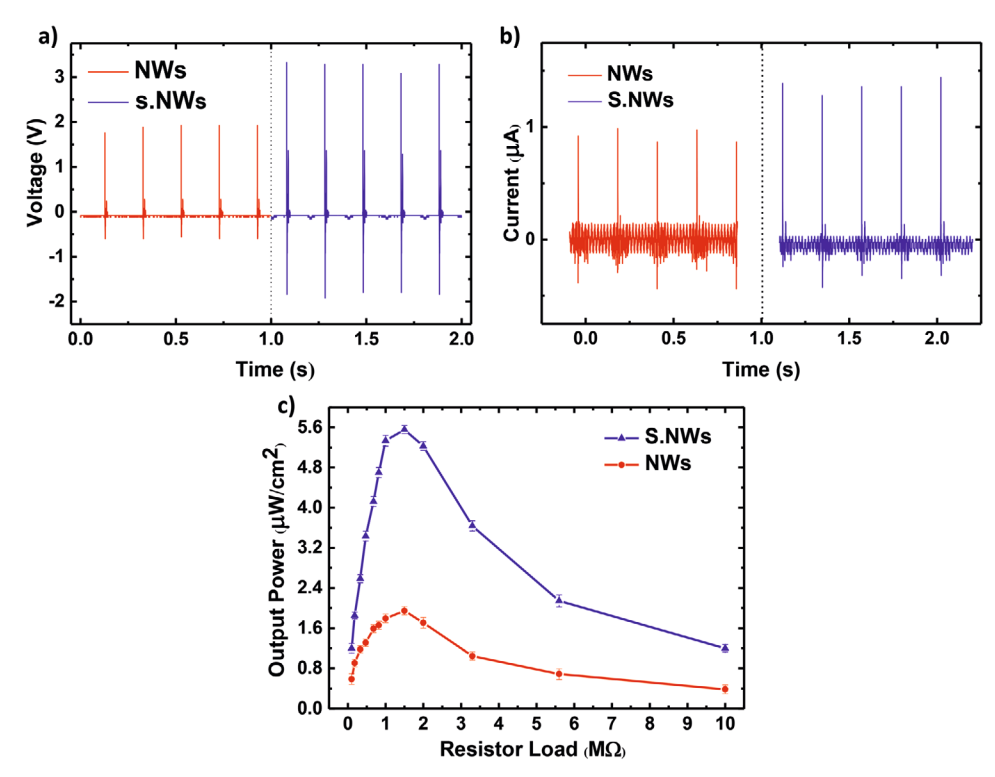


Figure 5. a) V_{oc} and b) I_{sc} of sausage-like nanowire and nanowire nanogenerators. All nanofiber layers experienced the same excitation with a mechanical force of 20 N. The cyclic response of the nanogenerators, V_{oc} , and I_{sc} , are given in impact frequency of 5 Hz. c) Power density of S.NWs and NWs nanogenerators measured across a range of load resistances.

method (FEM) modeling is performed. To this end, we generated both smooth and sausage-type morphologies to allow for internal comparison (see Figure 6). We note that for these FEM simulations, the morphologies have been generated only to resemble the experimental observations. Since in contrast to the calculations discussed above structure formation is not the purpose of this second set of simulations, the morphologies should not be compared one-to-one to the ones resulting from our multiphase model given in Figure 3. Details of the FEM simulations are presented in Section S7, Supporting Information. The piezoelectric voltage and volumetric strain are simulated when a 2×10^{-4} N force is applied in the direction of the nanowire length. Figure 6 shows the piezoelectric voltage and deformation of S.NWS and NWS samples. The S.NWs and NWs nanogenerators generate a piezoelectric voltage of 1 and 0.7 V, respectively. Interestingly, FEM suggests a higher piezoelectric voltage of sausage nanowires. An important parameter that affects the piezoelectric voltage is the deformability of

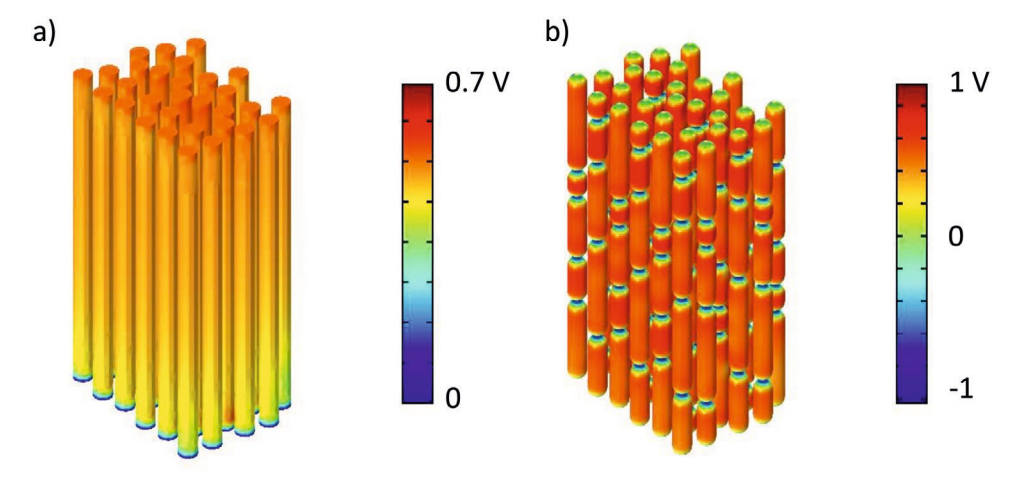


Figure 6. Simulated piezoelectric voltage for a) normal nanowires, b) sausage-like nanowires. Samples are impacted by a 2×10^{-4} N pulse in the stress-charge mode.



www.advmatinterfaces de

piezoelectric material. Equation (7) demonstrates the dependence of piezoelectric charge coefficient d_{33} , to the ratio of variation in applied force to change in surface charge as follows:

$$d_{33} = \frac{\partial P}{\partial \sigma_3} = P \left[\frac{\partial ln\mu}{\partial \sigma_3} - \frac{\partial lnz}{\partial \sigma_3} \right] \tag{7}$$

Where σ_3 is the surface charge, μ is total dipole, z is the thickness, and $P=\frac{\mu}{\text{volume}}$ is the polarization. The first term of Equation (7) is associated with the number of dipoles present at a constant thickness. The second term is connected to the deformability of the piezoelectric material which is associated with the volumetric strain. FEM results in volumetric strain values of 0.011 and 0.008 for S.NWs and NWs, under the same 2×10^{-4} N pulse, respectively. Movie S7, Supporting Information, clearly shows that for the sausage structure, the conjunction between each block undergoes higher strain and consequently higher deformation.

Since the crystallinity of NWs and S.NWs is similar, the finite element analysis shows that the superior piezoelectric performance of the latter specimen is predominantly due to a higher deformability of the sausage-like nanostructures in comparison to smooth wires.

3. Conclusions

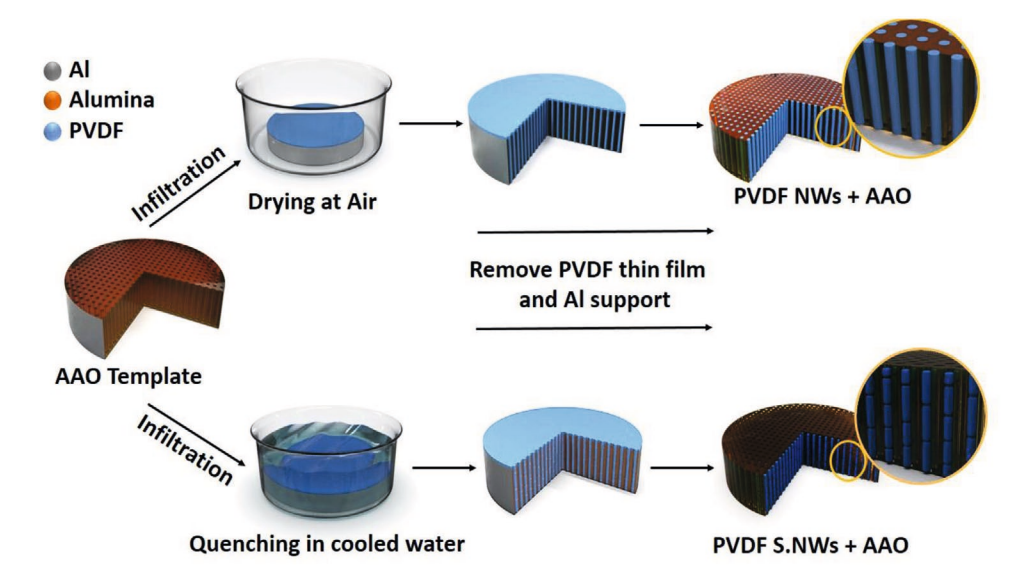
Solvent-nonsolvent phase-inversion has been combined with the nanopore-template-wetting technique to create a new type of piezoelectric PVDF nanowire morphology with a "sausage-like" appearance. The mechanism of formation of these nanostructures has been elucidated using dynamic out-ofequilibrium phase-field simulations. During the calculations, water is allowed to diffuse into the nanopores containing the polymer solution. Similar sausage-like structures as in the

experiment are obtained if it is assumed that the pore wall effectively repels the polymer. The simulations suggest that the average domain size decreases with the degree of confinement, in agreement with the experimentally observed trend. Varying the polymer concentration affects structure size as well, and also determines the likelihood that the domains remain connected in the dry specimen or break apart into separate entities. Our detailed simulation of such a complex system is of paramount importance in designing a new generation of PNGs. We have furthermore demonstrated that the sausage-like structures exhibit a much higher piezoelectric power output compared to normal "smooth" nanowires produced in the absence of phase inversion. With the aid of finite element simulations, we have shown that the higher deformability of the sausage-like nanogenerators is responsible for the strongly enhanced piezoelectric output. In summary, we have introduced and explored a new, cost-effective, and scalable approach towards fully novel and optimized polymeric piezoelectric nanostructures for efficient energy harvesting and sensing. In this explorative work, we have focused on the performance of these novel sausage-like PVDF nanowires, as well as giving qualitative explanations for the phenomena associated with processing and measuring. As an outlook, systematic variation and optimization of experimental and processing parameters, as well as extended characterization, will be subject to forthcoming studies.

4. Experimental Section

Materials: PVDF ($M_w = 275~000~g~mol^{-1}$), high purity (99.999%) Al foil with a thickness of 0.3 mm, Polydimethylsiloxane (PDMS) sylgard, ethanol, perchloric acid, and phosphoric acid were purchased from Sigma-Aldrich. DMF was purchased from Merck, Inc. All materials were used as received

Fabrication of Templates: AAO templates were fabricated under hard anodization (HA) conditions (Section S1, Supporting Information) and characterized using 0.3 M oxalic acid by applying an anodization voltage of 130 V. Before the anodization process, Al foil was ultrasonically



Scheme 1. Schematic representation of template-wetting method.

21967373, 2021, 5, Downloaded from https://onlinelibrary.wiely.com/doi/10.1002/admi.202001734 by Egyptian National Sti. Network (Bustinet), Wiley Online Library on [12.032023]. See the Terms and Conditions (https://onlinelibrary.wiely.com/terms-and-conditions) on Wiley Online Library for rules of use; OA articles are governed by the applicable Creative Commons License



www.advmatinterfaces.de

cleaned in acetone, washed in distilled water, and then dried at room temperature. To remove the surface roughness, the Al foil was electropolished in a mixed solution containing ethanol/perchloric acid (4/1) at 5 °C and 20 V for 4 min. Subsequently, a mild anodization process was carried out at 40 V for 300 s; afterward, in a HA condition the voltage increased to 130 V. Anodization process was performed in a 0 °C cooling bath to prevent burning and breakdown of the Al. Finally, the resulting templates were subjected to a widening process for 60, 80, and 100 min using 0.3 м phosphoric acid at 30 °C, to increase the nanopore diameters.

Fabrication of the Nanowires: For template-wetting, the AAO templates (68µm depth) were immersed into the PVDF/DMF 20 wt% solution at 60 °C for 20 h, ensuring the complete infiltration. Afterward, for efficient phase inversion, the template was immediately immersed in a deionized water bath at 0 °C, for 30 min (S.NWs sample). To obtain normal nanowires (NWs sample), templates were left at 60 °C overnight to allow for complete evaporation of the solvent. A residual 10 µm film remaining on the surface of the AAO templates was removed by mechanical polishing. The schematic representation of the nanowire production process is shown in **Scheme 1**.

Scanning Electron Microscope (SEM): Nanowires were sputter-coated with gold before SEM imaging. FESEM, Mira 2-XMU was employed to observe the top and cross-sectional view of the nanowires. For cross-section imaging, templates were broken at room temperature. The mean diameters of the nanowires and length of the sausage stacks were measured using Image] processing software.

FTIR Spectroscopy: A Bruker Tensor FT-IR Spectrometer equipped with Platinium ATR unit was used for polymorphism analysis. Measurements were performed with an average of 64 scans in the range of 400–4000 cm⁻¹ using a resolution of 4 cm⁻¹.

Differential Scanning Calorimetry (DSC): The crystallinity of the nanowires was measured utilizing a Mettler Toledo calorimeter. DSC measurements were performed from 25 to 200 °C with a heating rate of $10~^{\circ}\text{C}$ min $^{-1}$ under an N_2 atmosphere.

Piezoelectric Measurements: Nanogenerators were prepared by sandwiching AAO templates filled with PVDF nanowires (diameter of 1 cm) between two aluminum foils. A custom-built cyclic impact device with a plastic hammer (see Section S8, Figure S9, Supporting Information) was employed to mechanically impact the nanogenerators at the frequency 5 Hz at an impact force of 20 N. A GW INSTEK GDS-2072E oscilloscope was utilized to measure the $V_{\rm oc}$. Various resistive loads were used to measure the $I_{\rm sc}$ and calculate optimum power.

Supporting Information

Supporting Information is available from the Wiley Online Library or from the author.

Acknowledgements

K.A. and M.H.A. acknowledge the Alexander von Humboldt Foundation for the funding provided in the framework of the Sofja Kovalevskaja Award, endowed by the Federal Ministry of Education and Research, Germany. M.M.A. would like to thank the Alexander von Humboldt Foundation for their financial support, the Max-Planck Institute for Polymer Research for technical support, and Prof. Paul W. M. Blom for fruitful discussion. Correction added on 23 February 2021, after first online publication: Projekt Deal funding statement has been added.

Open access funding enabled and organized by Projekt DEAL.

Conflict of Interest

The authors declare no conflict of interest.

Keywords

nano-confinement, nanogenerators, nanowires, phase inversion, piezoelectric, template-wetting

Received: October 9, 2020 Revised: November 24, 2020 Published online: January 6, 2021

- [1] P. Seuwou, E. Banissi, G. Ubakanma, Digital Twin Technologies and Smart Cities, Springer, Cham 2020, pp. 37-52.
- [2] B. C.-K. Tee, A. Chortos, A. Berndt, A. K. Nguyen, A. Tom, A. McGuire, Z. C. Lin, K. Tien, W.-G. Bae, H. Wang, P. Mei, H.-H. Chou, B. Cui, K. Deisseroth, T. N. Ng, Z. Bao, *Science* 2015, 350, 313
- [3] Z. Jiang, M. O. G. Nayeem, K. Fukuda, S. Ding, H. Jin, T. Yokota, D. Inoue, D. Hashizume, T. Someya, Adv. Mater. 2019, 31, 1903446.
- [4] L. Dejace, N. Laubeuf, I. Furfaro, S. P. Lacour, Adv. Intell. Syst. 2019, 1, 1900079.
- [5] Z. L. Wang, J. Song, Science 2006, 312, 242.
- [6] T. Yang, H. Pan, G. Tian, B. Zhang, D. Xiong, Y. Gao, L. Zhang, Nano Energy 2020, 72, 104706.
- [7] G. Tian, D. Xiong, Y. Su, T. Yang, Y. Gao, C. Yan, Wang, Nano Lett. 2020, 20, 4270.
- [8] C. H. Wang, W. S. Liao, Z. H. Lin, N. J. Ku, Y. C. Li, Y. C. Chen, Z. L. Wang, C. P. Liu, Adv. Energy Mater. 2014, 4, 1400392.
- [9] J. Yan, Y. G. Jeong, ACS Appl. Mater. Interfaces 2016, 8, 15700.
- [10] X. Chen, S. Xu, N. Yao, Y. Shi, Nano Lett. 2010, 10, 2133.
- [11] S. Anwar, M. Hassanpour Amiri, S. Jiang, M. M. Abolhasani, P. R. Rocha, K. Asadi, Adv. Funct. Mater. 2020, 2004326, https://doi. org/10.1002/adfm.202004326.
- [12] A. Datta, Y. S. Choi, E. Chalmers, C. Ou, S. Kar-Narayan, Adv. Funct. Mater. 2017, 27, 1604262.
- [13] M. M. Abolhasani, K. Shirvanimoghaddam, M. Naebe, Compos. Sci. Technol. 2017. 138. 49.
- [14] M. Li, H. J. Wondergem, M.-J. Spijkman, K. Asadi, I. Katsouras, P. W. M. Blom, D. M. de Leeuw, *Nat. Mater.* 2013, *12*, 433.
- [15] K. Asadi, D. M. de Leeuw, B. de Boer, P. W. M. Blom, *Nat. Mater.*
- [16] V. Khikhlovskyi, A. V. Gorbunova, A. J. J. M. van Breemen, R. A. J. Janssen, G. H. Gelinck, M. Kemerink, Org. Electron. 2013, 14, 2300.
- [17] A. J. J. M. van Breemen, T. Zaba, V. Khikhlovskyi, J. J. Michels, R. A. J. Janssen, M. Kemerink, G. H. Gelinck, Adv. Funct. Mater. 2014, 25, 278;
- [18] L. Bernard, V. Khikhlovskyi, A. van Breemen, J. J. Michels, R. Janssen, M. Kemerink, G. Gelinck, N. Pilet, *Org. Electron.* 2018, 53, 242.
- [19] M. M. Abolhasani, K. Shirvanimoghaddam, H. Khayyam, S. M. Moosavi, N. Zohdi, M. Naebe, *Polym. Test.* 2018, 66, 178.
- [20] S. Tu, Q. Jiang, X. Zhang, H. N. Alshareef, ACS Nano 2018, 12, 3369.
- [21] M. M. Abolhasani, M. Naebe, K. Shirvanimoghaddam, H. Fashandi, H. Khayyam, M. Joordens, A. Pipertzis, S. Anwar, R. Berger, G. Floudas, *Nano Energy* 2019, 62, 594.
- [22] M. M. Abolhasani, M. Ashjari, S. Azimi, H. Fashandi, *Mater. Chem. Phys.* 2016, 217, 543.
- [23] M. Baqeri, M. M. Abolhasani, M. R. Mozdianfard, Q. Guo, A. Oroumei, M. Naebe, J. Appl. Polym. Sci. 2015, 132, 42304.
- [24] M. Baniasadi, J. Huang, Z. Xu, S. Moreno, X. Yang, J. Chang, M. A. Quevedo-Lopez, M. Naraghi, M. Minary-Jolandan, ACS Appl. Mater. Interfaces 2015, 7, 5358.
- [25] I. Katsouras, K. Asadi, M. Li, T. B. Van Driel, K. S. Kjaer, D. Zhao, T. Lenz, Y. Gu, P. W. Blom, D. Damjanovic, *Nat. Mater.* 2016, 15, 78.





www.advmatinterfaces.de

- [26] J. Martín, D. Zhao, T. Lenz, I. Katsouras, D. M. de Leeuw, N. Stingelin, *Mater. Horiz.* 2017, 4, 408.
- [27] P. Sajkiewicz, A. Wasiak, Z. Gocłowski, Euro. Polym. J. 1999, 35, 423.
- [28] C. Zhang, Y. Fan, H. Li, Y. Li, L. Zhang, S. Cao, S. Kuang, Y. Zhao, A. Chen, G. Zhu, ACS Nano 2018, 12, 4803.
- [29] J. Chang, M. Dommer, C. Chang, L. Lin, Nano Energy 2012, 1, 356.
- [30] T. Huang, C. Wang, H. Yu, H. Wang, Q. Zhang, M. Zhu, Nano Energy 2015, 14, 226.
- [31] X. Liu, J. Ma, X. Wu, L. Lin, X. Wang, ACS Nano 2017, 11, 1901.
- [32] C. Chang, V. H. Tran, J. Wang, Y.-K. Fuh, L. Lin, Nano. Lett. 2010, 10, 726.
- [33] H. Jin, M. O. G. Nayeem, S. Lee, N. Matsuhisa, D. Inoue, T. Yokota, D. Hashizume, T. Someya, ACS Nano 2019, 13, 7905.
- [34] A. Lund, K. Rundqvist, E. Nilsson, L. Yu, B. Hagström, C. Müller, npj Flexible Electron. 2018, 2, 9.
- [35] G. Tian, W. Deng, Y. Gao, D. Xiong, C. Yan, X. He, W. Yan, Nano Energy 2019, 59, 574.
- [36] R. A. Whiter, V. Narayan, S. Kar-Narayan, Adv. Energy Mater. 2014, 4, 1400519.
- [37] V. Cauda, S. Stassi, K. Bejtka, G. Canavese, ACS Appl. Mater. Interfaces 2013, 5, 6430.
- [38] V. Cauda, B. Torre, A. Falqui, G. Canavese, S. Stassi, T. Bein, M. Pizzi, Chem. Mater. 2012, 24, 4215.
- [39] N. Soin, D. Boyer, K. Prashanthi, S. Sharma, A. A. Narasimulu, J. Luo, T. H. Shah, E. Siores, T. Thundat, *Chem. Commun.* 2015, 51, 8257
- [40] M. Zhang, A.-Q. Zhang, B.-K. Zhu, C.-H. Du, Y.-Y. Xu, J. Membr. Sci. 2008, 319, 169.
- [41] R. A. Whiter, Y. Calahorra, C. Ou, S. Kar-Narayan, Macromol. Mater. Eng. 2016, 301, 1016.
- [42] H. S. Dehsari, J. J. Michels, K. Asadi, J. Mater. Chem. 2017, 5, 10490.

- [43] M. M. Abolhasani, M. Naebe, M. Hassanpour Amiri, K. Shirvanimoghaddam, S. Anwar, J. J. Michels, K. Asadi, Adv. Sci. 2020, 7, 2000517.
- [44] J. T. Jung, J. F. Kim, H. H. Wang, E. Di Nicolo, E. Drioli, Y. M. Lee, J. Membr. Sci. 2016, 514, 250.
- [45] S. Kouijzer, J. J. Michels, M. van den Berg, V. S. Gevaerts, M. Turbiez, M. M. Wienk, R. A. Janssen, J. Am. Chem. Soc. 2013, 135, 12057.
- [46] J. J. Michels, E. Moons, Macromolecules 2013, 46, 8693.
- [47] C. Schaefer, P. van der Schoot, J. J. Michels, Phys. Rev. 2015, 91, 022602.
- [48] C. Schaefer, J. J. Michels, P. van der Schoot, Macromolecules 2016, 49, 6858.
- [49] C. Schaefer, J. J. Michels, P. van der Schoot, Macromolecules 2017, 50, 5914.
- [50] J. J. Michels, K. Zhang, P. Wucher, P. M. Beaujuge, W. Pisula, T. Marszalek, Nat. Mater. 2020, 20, 68.
- [51] K. Binder, H. Frisch, Z. Phys. B 1991, 84, 403.
- [52] S. Puri, K. Binder, Phys. Rev. 1994, 49, 2178.
- [53] A. Silberberg, J. Chem. Phys. 1968, 48, 2835.
- [54] M. Ariyapadi, E. Nauman, J. Polym. Sci., Part B: Polym. Phys. 1990, 28 2395
- [55] P.-G. De Gennes, F. Brochard-Wyart, D. Quéré, Capillarity and wetting phenomena: drops, bubbles, pearls, waves, Springer Science & Business Media, New York 2013.
- [56] X. Li, Y. Wang, X. Lu, C. Xiao, J. Membr. Sci. 2008, 320, 477.
- [57] L. Swallow, J. Luo, E. Siores, I. Patel, D. Dodds, Smart Mater. Struct. 2008, 17, 025017.
- [58] A. Sultana, S. K. Ghosh, M. M. Alam, P. Sadhukhan, K. Roy, M. Xie, D. Mandal, ACS Appl. Mater. Interfaces 2019, 11, 27279